High Fidelity Modeling and Experiments to Inform Safety Analysis Codes for Heat Pipe Microreactors

Carolina Bourdot Dutra,[*,a] Elia Merzari,[a,e] John Acierno,[a] Adam Kraus,[a] Annalisa Manera,[b,c,d] Victor Petrov,[b,c,d] Taehwan Ahn,[b] Pei-Hsun Huang,[b] and Dillon Shaver[e]

[a] *Pennsylvania State University, Ken and Mary Alice Lindquist Department of Nuclear Engineering 205 Hallowell Bldg, University Park, PA 16802, USA*

[b] *University of Michigan, Department of Nuclear Engineering & Radiological Sciences 2355 Bonisteel Blvd, Ann Arbor, MI 48109, USA*

[c] *ETH Zurich, Department of Mechanical and Process Engineering Sonneggstrasse 3, 8092, Zurich, Switzerland*

[d] *Paul Scherrer Institute, Laboratory for Reactor Physics and Thermal-Hydraulics (LRT) 5232 Villigen PSI, Switzerland*

[e] *Argonne National Laboratory, Nuclear Science and Engineering Division 9700 S. Cass Avenue, Lemont, IL 60439, USA*

[*]Email: cdutra@psu.edu

Number of pages: 44

Number of tables: 9

Number of figures: 27

Abstract

Heat pipe micro-reactors are reactor designs that primarily use liquid metal heat pipes to cool the core. The main interest in heat pipes relies on the fact that they can remove heat passively. This, along with the use of liquid metal, allows the reactor to operate at higher temperatures. Although the use of heat pipes in nuclear reactors is new, liquid metal heat pipe technology is mature. Nevertheless, experimental data on heat pipes are scarce, and very little is known about their behavior during abnormal operations and close to their thermal limits. Therefore, new experiments and accurate heat pipe simulations are needed to develop reliable closure models. This work describes a joint experimental and numerical investigation into heat pipes that attempts an initial closure of this gap. The numerical and experimental efforts are currently proceeding *in parallel*, aiming at different aspects of heat pipes. The numerical part is focused on gaps in local closures, and the experiments captured an overall heat pipe behavior.

Keywords — Microreactor, Sodium Heat Pipe, Experiments, CFD, Volume of Fluid

I. INTRODUCTION

Microreactors, also known as very-Small Modular Reactors (vSMRs) or Special Purpose Reactors (SPRs), are being considered for use in unique applications where other methods of megawatt level energy production are uneconomical or unavailable [1]. These reactors produce a few MW of power (typically < 20 MW), and can be manufactured in a factory and then transported by truck, train, plane, or ship to the deployment location. They are designed for fully- or semi-autonomous operation to be used for electricity production in remote locations, military installations, industrial applications such as desalination or hydrogen production, or integration in micro-grids [2]. The designs can be classified into two main categories: high-temperature gas reactors (HTGRs) and heat pipe reactors, the latter being the focus of the current work. These reactor designs foresee using liquid metal heat pipes based on sodium (Na), potassium (K), or NaK as working fluid [3]. The main advantages of liquid metal heat pipes are that they can operate at very high temperatures and are entirely passive heat removal devices. Their heat transfer capabilities are superior to solid metal devices with the exact dimensions [4].

A heat pipe is a sealed tube containing a wick structure attached to the inner surface and a working fluid, which transports heat continuously from one end to another by capillary pressure, as shown in Figure 1. It is comprised of three parts: an evaporator, an adiabatic section, and a condenser.

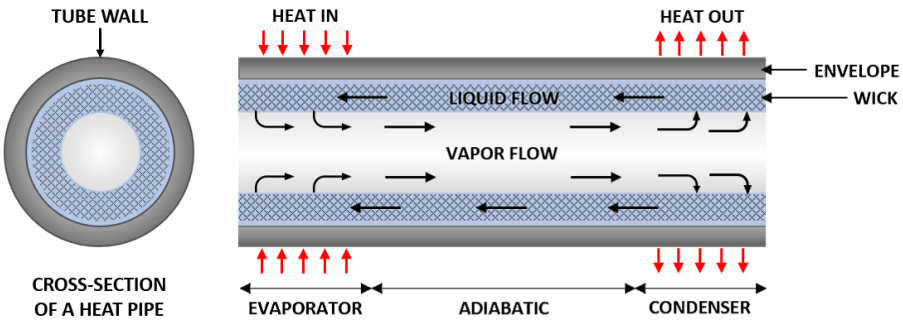

Fig. 1. Scheme of the heat pipe operation

Although liquid metal heat pipe technology is mature [5], the use of heat pipes in the cooling of nuclear reactors is still new. Hence, the development of accurate heat pipe simulation capabilities is required. Several works performed simulations with two-phase models and a porous medium approach to model the wick structure [6], [7], [8]. More recently, a 1D two-phase formulation

has been developed in the Nuclear Energy Advanced Modeling and Simulation code Sockeye [9]. However, the need for closure models and high-resolution experimental data was recognized as it is needed to gain insight into the behavior of the heat pipes and validate the computational approaches.

Experimental data on heat pipes exist mainly for nominal operation conditions and do not present the spatial resolution suitable for validating high-fidelity simulations. In addition, very little is known about the behavior of heat pipes during abnormal operation and close to the heat pipes' thermal limits. Therefore, new experimental data is needed to further develop and validate thermal-hydraulics codes that can be used to license heat pipe micro-reactors.

Given the difficulty in obtaining a complete picture of the complex internal physics of heat pipes, numerical simulation plays an essential role in complementing the knowledge extracted from experiments alone. In fact, complete closure information cannot be obtained by experimentation due to the difficulty of measuring and visualizing the flow and heat transfer behavior inside heat pipes.

Several works to investigate the heat pipe performance were carried out. Two examples are from Bodla et al. [10] [11], who reconstructed CT scanned samples of porous sintered wicks to produce high-quality finite-volume meshes representing the solid and fluid regions. First, they performed a conjugated heat transfer analysis to obtain the effective thermal conductivity. Then, they used the Volume of Fluid (VOF) approach to obtain information about the wick. The works of Kempers et al. [12] and Chen et al. [13] highlight the importance of developing accurate models to account for the evaporation characteristics within the wick.

While a considerable amount of research has been dedicated to the detailed modeling and simulation of heat pipes, it was primarily concerned with normal operation using water [10] [11] [14] [15]. Most of the numerical models tend to ignore the phenomena occurring outside this range. We focus on developing models that can accurately represent behavior at operational conditions relevant to micro-reactors and near the five operational limits: viscous, sonic, capillary, entrainment/flooding, and boiling.

This work presents a combined experimental - Section II - and numerical study - Section III and IV - which is currently proceeding *in parallel*, aiming at different aspects of heat pipes. While the numerical campaign targets gaps in local closures, the experiments focus on overall heat pipe

behavior. Finally, the newly developed correlations are utilized within the modeling code Sockeye [9] - in Section V - to reproduce the experiments.

For the first stage of this program, we perform high-resolution experiments on sodium heat pipes and high-resolution single-phase, and volume of fluid [16] simulations in the heat pipe wick. Then, the information from these studies is combined to build a 2-D model of the heat pipe. In particular:

- A series of novel experiments are described and conducted in Section II.
- Parametric VOF simulations are performed to obtain the interface shape and the capillary pressure in the wick structure. Results are discussed in Section III.
- Information from the VOF simulations is used to perform single-phase simulations to evaluate correlations for the liquid flow in the representative wick structure. Results are discussed in Section IV.
- A 2-D heat pipe model was validated using information from the previous sections, and evaluations of the capillary limit are presented in Section V.

We emphasize that the high resolution simulations are used to extract relevant closure information such as capillary pressure, meniscus shape, and friction factors. Heat transfer calculations are also conducted to obtain information about interfacial and wall heat transfer. Again, the focus is on the liquid flow within the wick. These results are used to reproduce the experiments using Sockeye and to evaluate the capillary limit.

II. EXPERIMENTS

Over the past few years, the University of Michigan (UM) has acquired 30 sodium heat pipes. The planned experimental campaign will feature high-resolution X-ray radiography and fiber-optics-enabled temperature measurements. As the starting point, a facility has been built instrumented with thermocouples. The facility is described below, and several steady-state and power transients are investigated. This data can be used to validate reduced-order codes such as Sockeye.

II.A. Experimental Setup

The sodium heat pipe (HP) was manufactured by Advanced Cooling Technologies Inc. (ACT) with a stainless-steel 304 tube (25.4 mm of outer diameter (OD), 1.75 mm of thickness, and 1,016 mm of length). Based on the manufacturer's specification, the sodium heat pipe's maximum power is 2.2 kW. According to ACT's heat pipe limit curve [17], the viscous and capillary limits dominated the operational range of the heat pipe used in this study. Figure 2 shows a schematic diagram of the test facility. The test section assembly consists of the evaporator (254 mm), adiabatic (508 mm), and condenser (254 mm) sections. For the evaporator section, the double spiral shaped silicon carbide (SiC) heater (52 mm of OD, 40 mm of ID, and 254 mm of heating length) was used to heat the heat pipe through radiational heat transfer with a maximum operable temperature of 1200°C. The material of the heater was selected with the consideration of a low Z-number to reduce the attenuation of X-rays for the radiography measurement. The heater was fixed to a support, as shown in Figure 2, and calcium silicate parts were used for the concentric alignment, protection of brittle heater, and electrical insulation. The heater was covered with mineral wool pipe insulation with 220 mm OD.

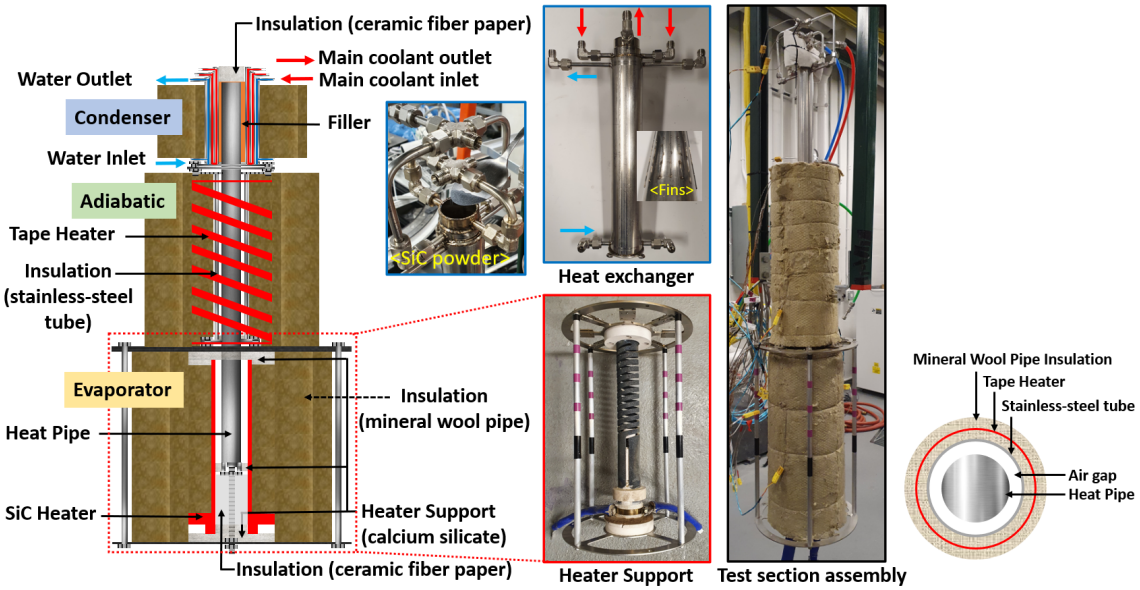

Fig. 2. Schematic diagram of a separate-effect test facility for a single sodium heat pipe, and cross-sectional view of the heat pipe [17] [18]

On the adiabatic section, the 31.75 mm OD stainless-steel tube (0.889 mm of thickness) was

installed to support the test section. The 2.286 mm air gap between the stainless-steel tube and the heat pipe acts as an insulator. In addition, a tape heater (500 W of maximum power) was installed at the outer surface of the inner layer insulation. The insulation temperature was controlled as same as the heat pipe wall temperature to eliminate the heat loss through the adiabatic section. Its radial cross-section view is shown in Figure 2.

A multi-channel annulus shell-type heat exchanger (HX) was fabricated with four 0.9 mm thick stainless steel tubes for the condenser section, as shown in Figure 2. With the double channel design, the main cooling fluid (usually air) is injected downward through the outermost layer and then discharged upward at the inner layer to guarantee a better uniformity of heat flux on the condenser section. The straight fins were welded at the surface of the inside double channel (0.7 mm gap) to enhance the heat transfer coefficient. In addition, the auxiliary water-cooling channel (2.3 mm gap) was applied to the outer layer of the HX. With the auxiliary water flow, the overall heat transfer rate was increased by lowering the temperature of the main cooling fluid. The heat loss can be negligible from the cold outer surface of the HX. Furthermore, the SiC powder was applied to the gap of 2.3 mm between the heat pipe and the HX to enhance the thermal conduction uniformly. The heat removal rate was calculated by enthalpy changes of both cooling fluids, as it follows:

$$Q_{hx} = c_{p,w}\dot{m}_w(T_{fw2} - T_{fw1}) + c_{p,a}\dot{m}_a(T_{fa2} - T_{fa1}), \tag{1}$$

where Q_{hx} is the heat transfer rate of the heat exchanger (W), c_p is the thermal capacity (J/kg^{o}C), $\dot{m}$ is the mass flow rate (kg/s), and T_f is the fluid temperature (^{o}C). The subscripts 1 and 2 represent the inlet and outlet, and a and w are air and water, respectively.

The piping and instrumentation diagram of the test facility is shown in Figure 3. The SiC heater was operated by PID controller with a silicon-controlled rectifier (SCR) based on the heating power or heater temperature.

The tape heater was also operated by PID controller with a contactor relay based on the temperature. Two-watt transducers (Ohio Semitronics – PC5) were used to measure those powers consumed in the heaters. The cooling fluid system was designed as two open-loop of air and water for the condenser section, and the mass flow rates were measured by two 3/8-inch Coriolis flow meters (Endress Hauser – ProMass). The test section was equipped with 39 ungrounded K-type thermocouples (TCs). 28 small-size high-accuracy TCs (0.5 mm OD sheathed – Watlow) were

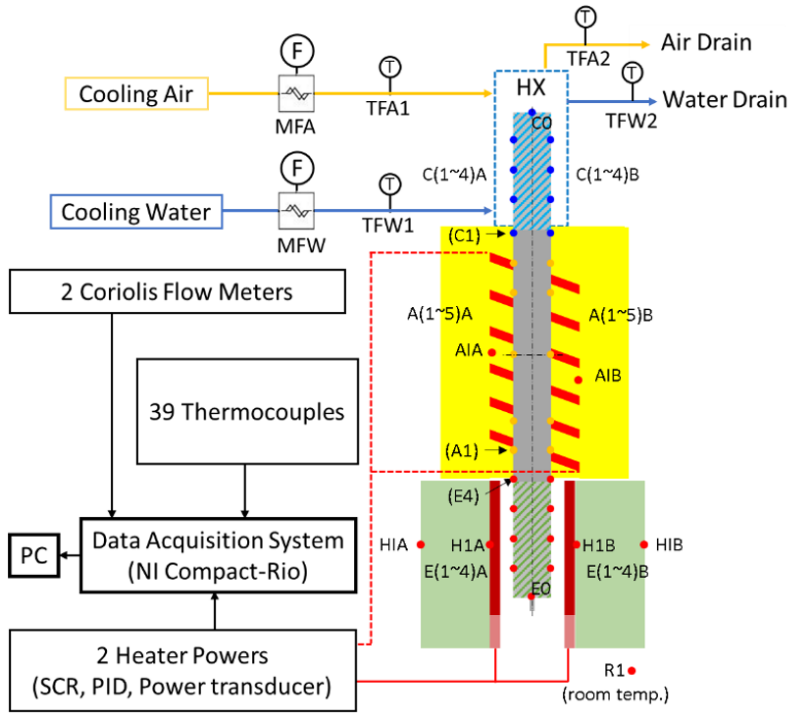

TC location (mm)	
C0	1016
C4(A/B)	952.5
C3(A/B)	889
C2(A/B)	825.5
C1(A/B)	762
A5(A/B)	698.5
A4(A/B)	635
A3(A/B)	508
A2(A/B)	381
A1(A/B)	317.5
E4(A/B)	254
E3(A/B)	190.5
E2(A/B)	127
E1(A/B)	63.5
E0	0

Fig. 3. Piping and instrumentation diagram and the locations of temperature measurement

used to measure the wall temperature of the heat pipe, and TCs were tied on the heat pipe surface with 0.5 mm stainless steel wires. The other 11 TCs (1.6 mm OD sheathed) were used to measure the SiC heater outer surface temperatures, the mineral wool pipe insulation surface temperatures, ambient temperature, and the inlet and outlet temperatures of cooling channels of air and water, respectively. All the data were acquired using a Compact Rio chassis (National Instruments™) and PC programmed with the LabVIEW.

The transients that have been investigated are relevant to heat pipe operation in microreactors. These include the startup and shutdown processes of the sodium heat pipe, which are essential to the successful operation of microreactors. Therefore, key parameters such as input power at the evaporator section, cooling condition at the condenser section, and heat pipe orientation serve an essential role in the performance of the heat pipe. Values have been selected to reflect reasonable operation regimes and transients [19].

II.B. Results

Table I summarizes the test conditions for Test-017, Test-018 and Test-026, and Tables II, III, and IV provides the parameters of each test. Test-018 was started from the hot state following the previous test. The wall temperature on the evaporator section oscillates in the heat pipe under vertical orientation (Test-017: Figure 4), which is related to the geyser boiling (GB) due to the excessive sodium charging amount [20], [21]. The GB is characterized by a nucleate pool boiling instability that occurs in the evaporator mainly under low heat fluxes [22]. When a large sodium reservoir is formed at the bottom of the evaporator section, a large vapor bubble intermittently detaches from the liquid pool, pushing the liquid sodium to the upper regions. The empty region at the evaporator is locally overheated until the liquid sodium return to the pool again. When geyser boiling occurs, the operational range of the heat pipe is significantly restricted due to the peak temperature of the evaporator. Moreover, repeated rapid temperature changes and vibrations can damage the heat pipe container and consequently affect the integrity of the entire cooling system of the reactor. Therefore, it is important to design and operate heat pipes under optimal performance to avoid geyser boiling.

Figure 4 (b) shows the steady-state temperature profile, including the amplitude of the temperature oscillation (min. and max. as the error bars). A large amplitude occurs at the evaporator section as the power increases. The temperature oscillation disappeared under the conditions of the horizontal orientation (Test-018: Figure 5) and the sufficiently high heater power (Test-026: Figure 6). Since the heater power was temporarily shut down to adjust the inclination from vertical (Test-017) to horizontal (Test-018), the HP wall temperature at region (1) dropped and recovered in Figure 4. As the system shuts down, the most remarkable temperature drop occurs at the condenser section (blue and red lines) due to the heat removal by HX.

TABLE I
Test conditions

Test no.	HP orientation	Maximum heater power	HX filler	HX cooling fluid	Initial condition
Test-017	Vertical	1.4 kW	Copper thread	Air+auxiliary water	Tw=20°C
Test-018	Horizontal	1.4 kW	Copper thread	Air+auxiliary water	Restart
Test-026*	Vertical	2.25 kW	SiC powder	Air	Restart
*A tape heater controlled by PID was used to minimize the heat loss at the adiabatic section					

TABLE II
The event scenario for Test-017

	End time (s)	Heater power (W)	Heat removal rate (W)	Mass flow rate of air (g/s)	Mass flow rate of water (g/s)
1	3777	500	174	0.6 – 1.9	-
2	4860	750	410	4	-
3	5359	1000	595	4.1 – 7	-
4	6671	1200	722	6.9	41
5	7070	1400	790	6.9	25

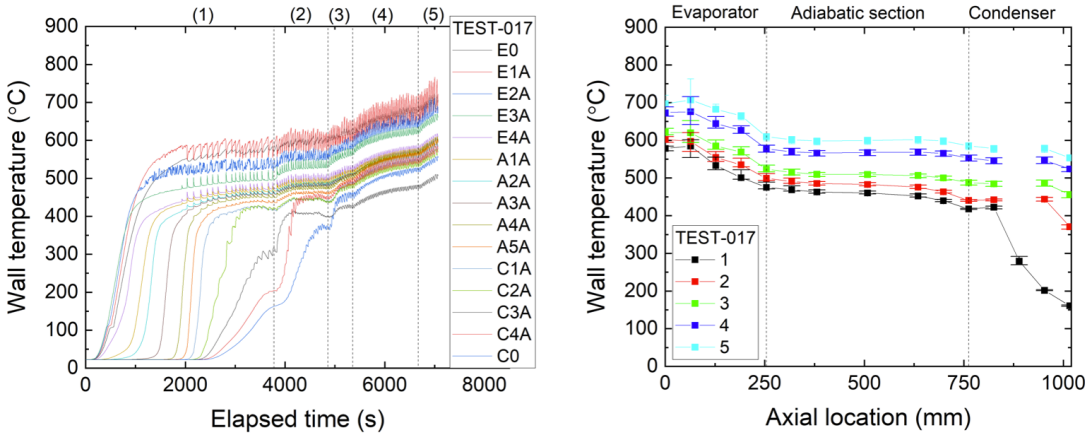

(a) (b)

Fig. 4. Result of Test-017: (a) the time series HP wall temperature (b) the axial distribution of the HP wall temperature under steady state

TABLE III
The event scenario for Test-018

	End time (s)	Heater power (W)	Heat removal rate (W)	Mass flow rate of air (g/s)	Mass flow rate of water (g/s)
1	902	750	387	3	32
2	1253	1000	451	3	33
3	1741	1200	700	2.9 – 5.8	33
4	2114	1400	764	5.8 – 7.6	33

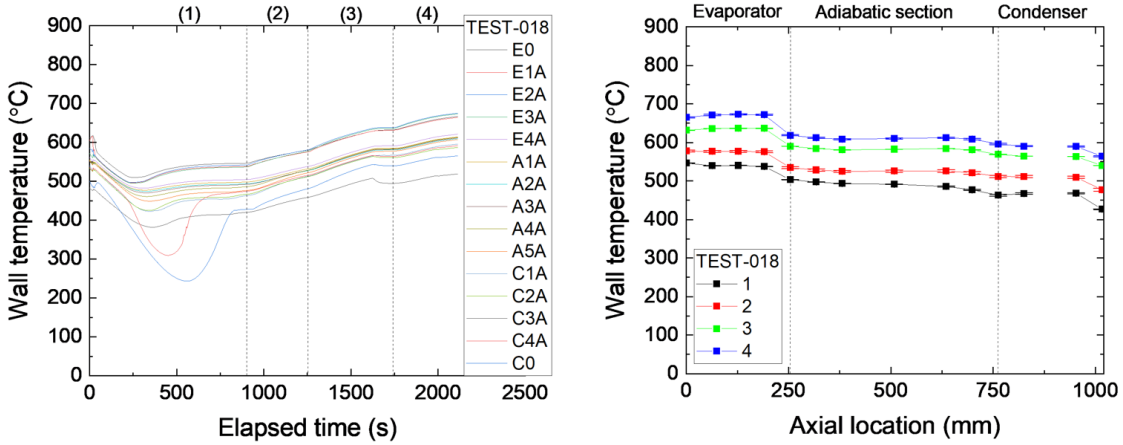

(a) (b)

Fig. 5. Result of Test-018: (a) the time series HP wall temperature (b) the axial distribution of the HP wall temperature under steady state

TABLE IV
The event scenario for Test-026

	End time (s)	Heater power (W)	Heat removal rate (W)	Mass flow rate of air (g/s)	Mass flow rate of water (g/s)
1	1832	500	207	1.9	-
2	3999	1000	468	1.9	-
3	5564	1500	1063	1.9 – 6.1	-
4	6600	2000	1353	6.7	-
5	8022	2250	1552	6.4	-

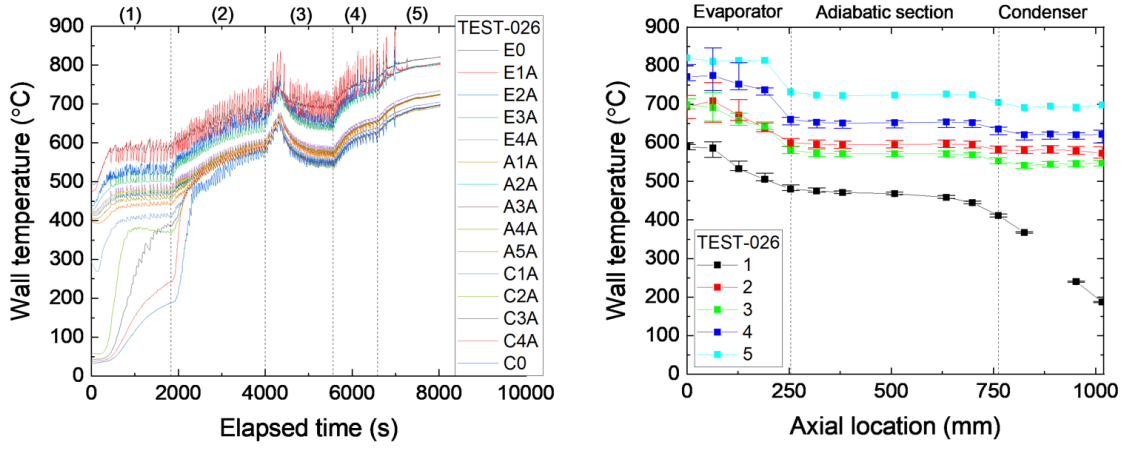

(a) (b)

Fig. 6. Result of Test-026: (a) the time series HP wall temperature (b) the axial distribution of the HP wall temperature under steady state

III. NUMERICAL SIMULATIONS: TWO-PHASE FLOW

The wick structure in heat pipes provides the capillary force that drives the circulation of the fluid; thus, it plays a crucial role in its thermal performance. In this work, we use the Volume of Fluid method [16] to model fluid flow in the wick region and extract relevant closure information, as it allows for direct resolution of the meniscus. Once the shape of the interface has been established, we conduct single-phase simulations that are used to evaluate different closures.

III.A. Methods

III.A.1. Wick modeling

Wicks can be produced from several materials, such as copper and stainless steel, and can be of different types, such as composite or homogeneous wicks. The last, is commonly made of screen mesh, which has lower capillary pressure and effective thermal conductivity but is simpler to manufacture. A screen mesh wick can be made with different geometries and configurations. To model a wick representative of the experimental model, a screen mesh with a wire diameter of 0.07 millimeters was woven using the CAD software Solidworks [23], as shown in Figure 7 (a), to obtain a mesh with three layers and 100 holes per inch. This wick will provide the capillary pressure needed to sustain the transport of the working fluid. The selected geometry is consistent with known designs. We note that the parameter choices will be refined once X-ray radiography becomes available. Moreover, several studies utilizing a screen mesh of 100 holes per inch indicated that this geometry provides better thermal performance [12] [24] [25] [26].

Afterward, in the ANSYS CAD software Spaceclaim, an enclosure was applied over the screen mesh to obtain a fluid domain, and the geometry was prepared to be meshed.

Then, a tetrahedral mesh was generated in ANSYS Meshing through the Patch Conforming Method, which is suitable for irregular geometries. It presented very good quality parameters, with minimum orthogonal quality above 0.3, maximum skewness below 0.95, and maximum aspect ratio below 15. This mesh was then converted into a polyhedral mesh in ANSYS Fluent to improve accuracy, as shown in Figure 8. That conversion significantly decreased the number of elements and increased the mesh quality.

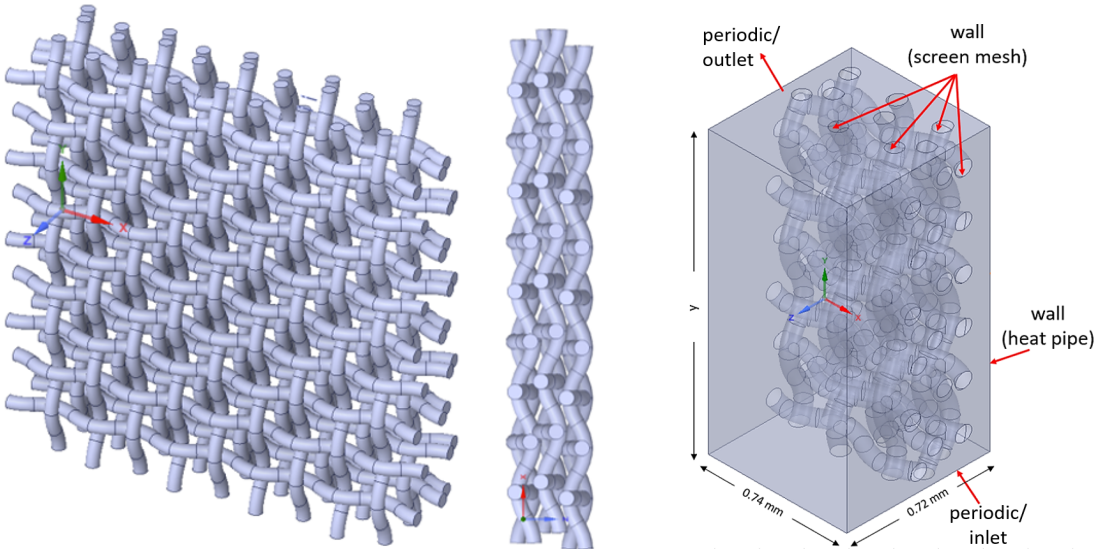

(a) (b)

Fig. 7. (a) Screen mesh model, (b) fluid domain with its boundary conditions.

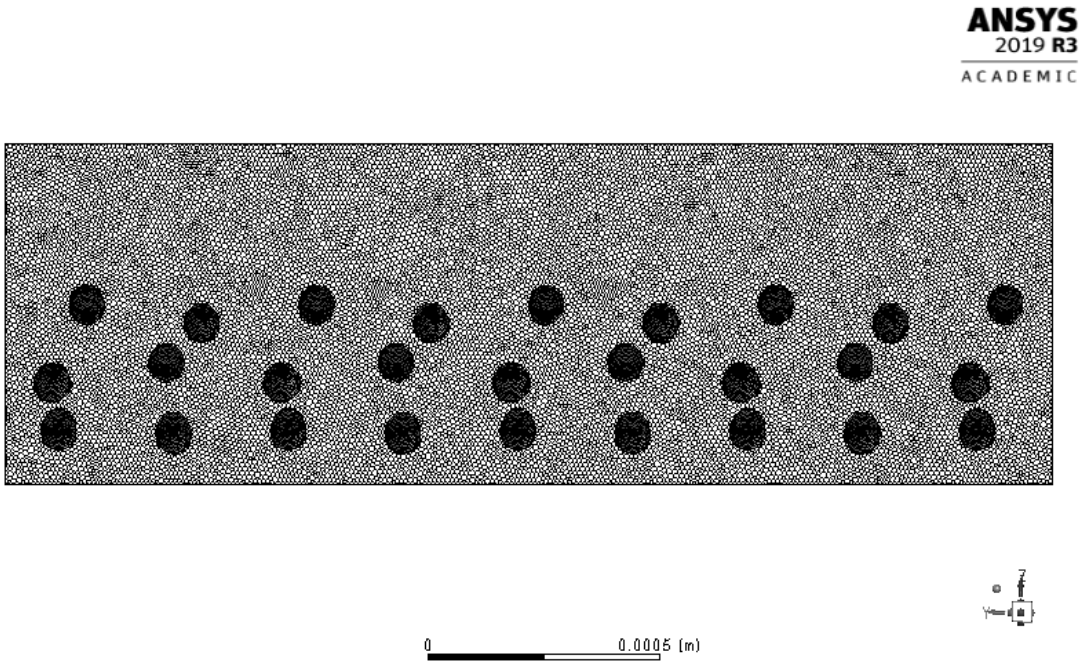

Fig. 8. Cross-section of the polyhedral mesh

III.A.2. Volume of Fluid approach

In this work, we use the VOF method available on ANSYS Fluent [27] [28]. The method models two immiscible fluids with a clearly defined interface through the Euler-Euler approach, which treats the phases as interpenetrating continua [29]. It is simpler than Euler-Lagrange models as it solves only a single set of equations.

The volume fraction of each phase is 0 or 1, except for the interface region, where there is a volume fraction for each additional phase within the computational cell. The volume fraction of the secondary phase, or in this case, the heavier phase, is defined as:

$$\alpha_l = \frac{V_l}{V} \tag{2}$$

where V denotes the total representative volume. Which lead us to three possible conditions:

- $\alpha_l = 0$: the cell is empty of liquid;
- $\alpha_l = 1$: the cell is full of liquid;
- $0 < \alpha_l < 1$: the cell contains the interface between the liquid and the vapor.

III.A.3. Model description

The VOF method is computationally expensive, limiting the size of the domain to a pore level. Thus, we use a domain representative of a small piece of the heat pipe, which is enough to provide the required information to build a closure model.

The chosen working fluid was water for the initial simulations, and the solid material was copper. These parameters were selected to mimic conditions similar to literature [10] and gain confidence in the methodology. The following boundary conditions for the domain represented in Figure 7 (a) were assumed: periodic at the streamwise direction; no-slip condition at the solid surface (walls); variable contact angle at the wall, characterizing a hydrophilic wall; symmetry condition at the remaining faces; adiabatic faces. We note that the vapor and the liquid flows were considered to have constant properties, and both were initially at saturated temperatures.

The geometric reconstruction scheme was used in the interface, which is the most accurate for unstructured meshes. This standard scheme uses a piecewise-linear approach to apply a special interpolation treatment to the cells near the two-phase interface. It assumes the interface between the fluids has a linear slope in each cell and uses this linear shape to calculate the advection of fluid through the face cells. The Pressure-velocity coupling scheme used was PISO [27].

For each VOF simulation, the domain was initialized with vapor patched at the middle and liquid in its remaining part. Then, the surface tension forces change the shape of the interface, and the capillary pressure changes in turn as well. A variable time-stepping method was used with a default value of the Global Courant number of 2. Due to the small mesh size needed to represent the meniscus shape and the velocity generated by the imbalances near the two-phase interface, the time-step was of an order of 10^{-6}. The simulations were monitored by tracking the area-weighted average pressure in a plane in the domain with the flow time. They were assumed to converge when the monitor stopped changing, and the residuals dropped below target values of 10^{-5}. For the preliminary simulations with water and copper, the surface tension was 0.072N/m. A sensitivity study on the contact angles between solid, liquid, and vapor was conducted for 60, 75, and 80 degrees.

The pressure as function of the position in a line across the domain is depicted in Figure 9 (a). As expected, there is a pressure jump between liquid and vapor across the interface, which is the capillary pressure. It is observed that the smaller the contact angle, the higher the capillary pressure, which agrees with the Young-Laplace Law. These results are consistent in trend and magnitude with available water results for porous wicks [11, 10], which yielded in one of the samples a capillary pressure of 302, and 537 Pa, for the contact angles of 75^o, and 60^o, respectively. Figure 9 (b) also presents a preliminary sensitivity conducted with water at the contact angle of 75 degrees, testing the domain length, types of mesh elements, and boundary conditions. The shortest domain tested was neglected for the subsequent simulations as it provided a capillary pressure more than 20% higher than the other simulations.

III.A.4. Mesh, domain, and boundary conditions sensitivity study

Once the setup was validated for the water cases, we developed models for the sodium heat pipes. This study and all the following simulations used sodium as the working fluid and steel as

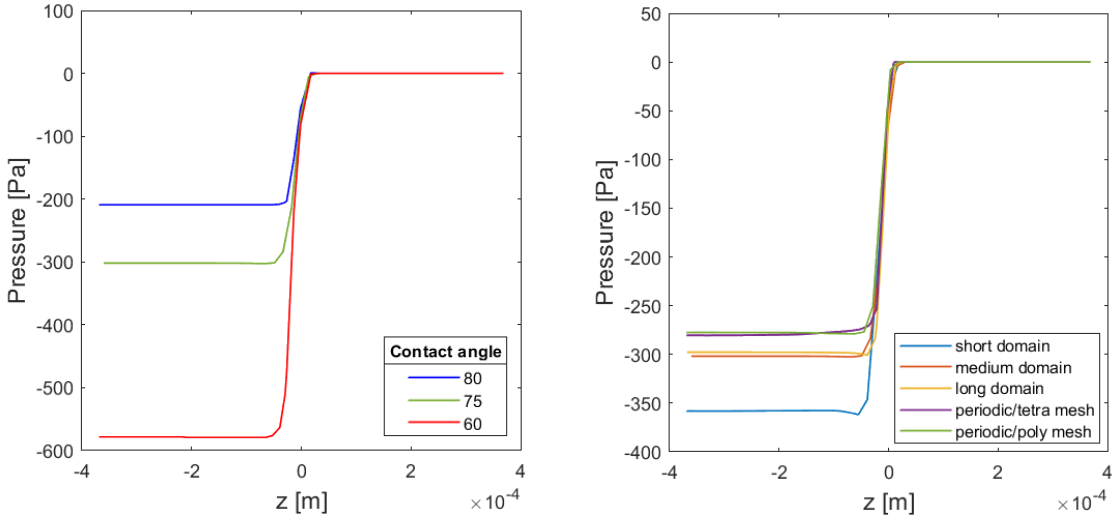

(a) (b)

Fig. 9. Pressure as a function of the position in a line across the domain for water: (a) with different contact angles, and (b) with different boundary conditions, mesh elements, and domain lengths

the solid material. Five meshes were generated to perform a mesh convergence study. The pressure as a function of the position and the relative error to the most refined mesh are shown in Figure 10 (a), and Table V, respectively. The capillary pressure was used as a parameter to compute the relative error to the most refined mesh. Mesh 1 was chosen due to its small error compared to Mesh 5 and, therefore, a good compromise between computational cost and accuracy. Besides, Mesh 1 and 5 are independent of each other regarding the number of elements.

TABLE V
Mesh convergence study

	Number of elements	Error (%)
Mesh 1	803434	3.14
Mesh 2	1031247	2.29
Mesh 3	1676200	1.85
Mesh 4	1782320	1.24
Mesh 5	3108326	—

Figure 10 (b) shows results of a subsequent domain length and a boundary condition convergence study performed, with the associated error displayed in Table VI. For the axial boundary

conditions, we examine two options: (1) a wall with a contact angle between solid-liquid-vapor of 90 degrees and (2) periodic boundaries. Moreover, the length of the domain was varied. The error is defined as the difference between each configuration and the case with periodic boundary conditions and longer length. The outcome of this study was the selection of the smaller domain and periodic boundary conditions to proceed with the simulations, as it provided reliable and faster results.

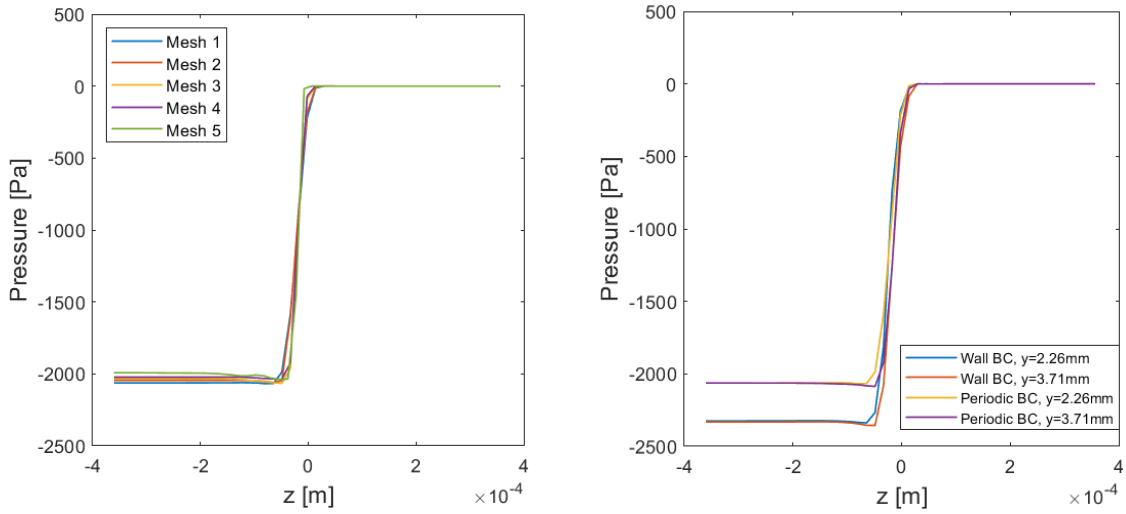

(a) (b)

Fig. 10. Mesh, domain and boundary conditions convergence study

TABLE VI
Boundary conditions and domain convergence study

Boundary Condition	Length of domain y (mm)	Capillary pressure (Pa)	Error (%)
Wall	2.26	2324.70	12.47
Wall	3.71	2332.30	12.83
Periodic	2.26	2062.45	0.22
Periodic	3.71	2067.05	—

III.A.5. Model setup

After getting reliable results for cases with water and completing the sensitivity study with sodium, we could begin our analysis. The contact angle of sodium on stainless steel is variable and

depends on the temperature [30], time [31], and pre-treatment [32] [33]. However, we consider only the changes caused by temperature in this work, using contact angles equivalent to temperatures ranging from 400 to 600 ^{o}C approximately. The smaller contact angles correspond to higher temperatures. In addition, the sodium properties and the surface tension varied for each contact angle, as they also depend on the temperature [34].

III.B. Results

An example of the vapor volume fraction and the isosurface of the liquid-vapor interface are presented in Figure 11, showing the respective meniscus shape that is formed.

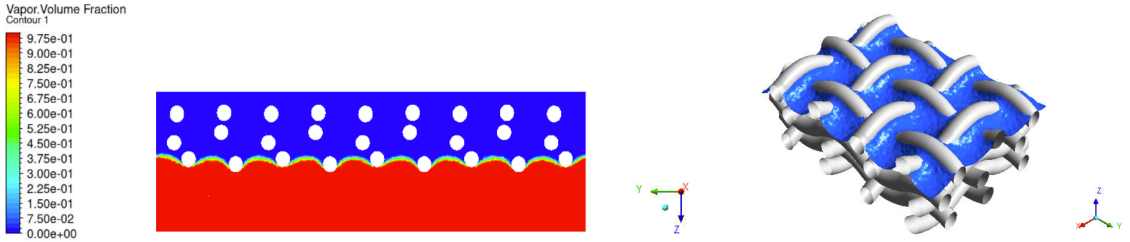

(a) (b)

Fig. 11. Vapor volume fraction (red) and isosurface of liquid-vapor interface

III.B.1. Capillary pressure and the meniscus shape

The capillary pressure as a function of the contact angle and the surface tension for each simulation is shown in Figure 12. Note that the surface tension is not a function of the contact angle, but both depend on the temperature. As the temperature changes, both contact angle and surface tension change. The capillary pressure observed at the liquid-vapor interface changes for each case due to the surface tension and the contact angle between fluid and solid. Again, it is observed that the smaller contact angles provide high capillary pressures.

Figure 13 compares the meniscus shapes for a small and a large contact angle, which illustrates the highly curved meniscus corresponding to the smaller contact angle and the nearly flat meniscus for the larger contact angle. These shapes were obtained through an isosurface of the two-phase interface.

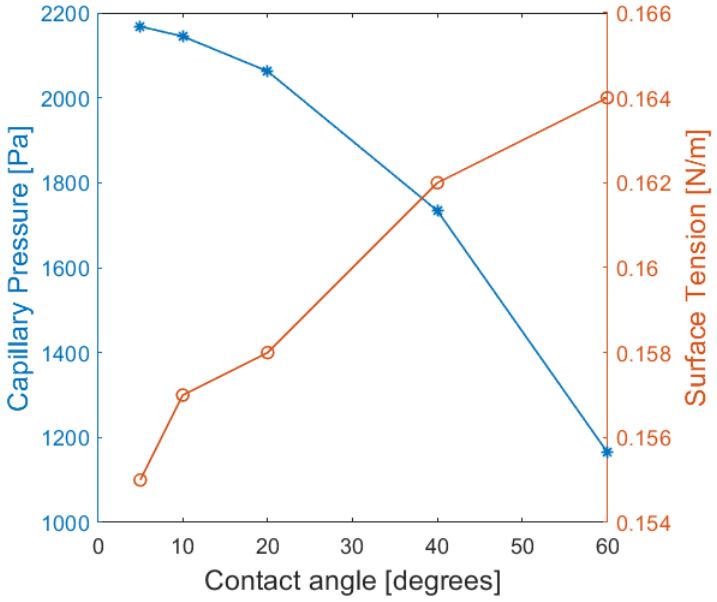

Fig. 12. Capillary pressure and surface tension as a function of the contact angle.

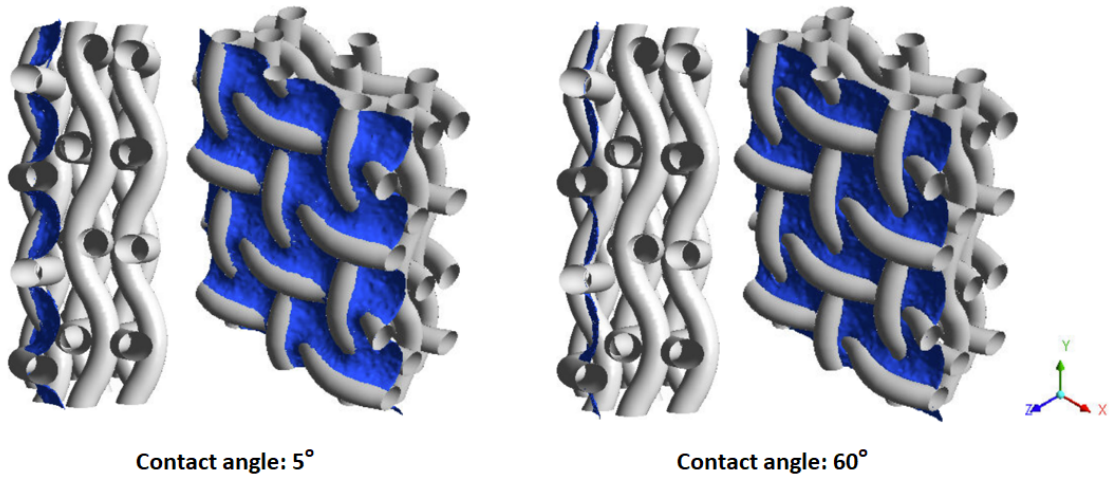

Fig. 13. Shape of the meniscus for the contact angles of 5 and 60 degrees, respectively

In subsequent analysis, the saturated liquid level in the wick was changed to verify the impact on changes in capillary pressure and meniscus shape, as shown in Figures 14 and 15. It can be seen that the meniscus shape and the capillary pressure change considerably with the saturation level in the wick. If the wick is completely filled with liquid, the capillary pressure rapidly drops

to zero, as expected, and the meniscus gets flat, as shown in Figure 15.

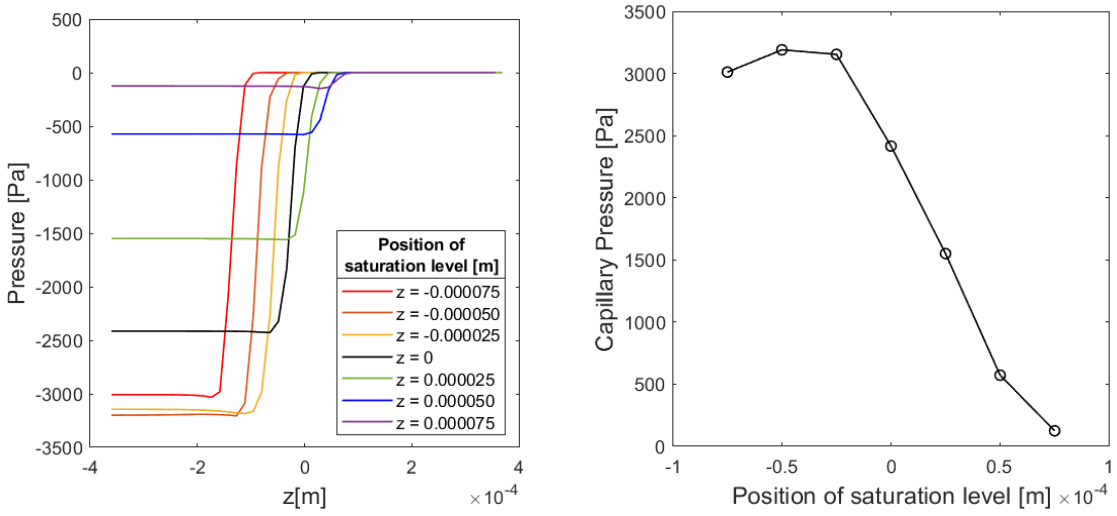

(a) (b)

Fig. 14. (a) Pressure as a function of the position in a line across the domain for different saturation levels, and (b) Capillary pressure as a function of the saturation level

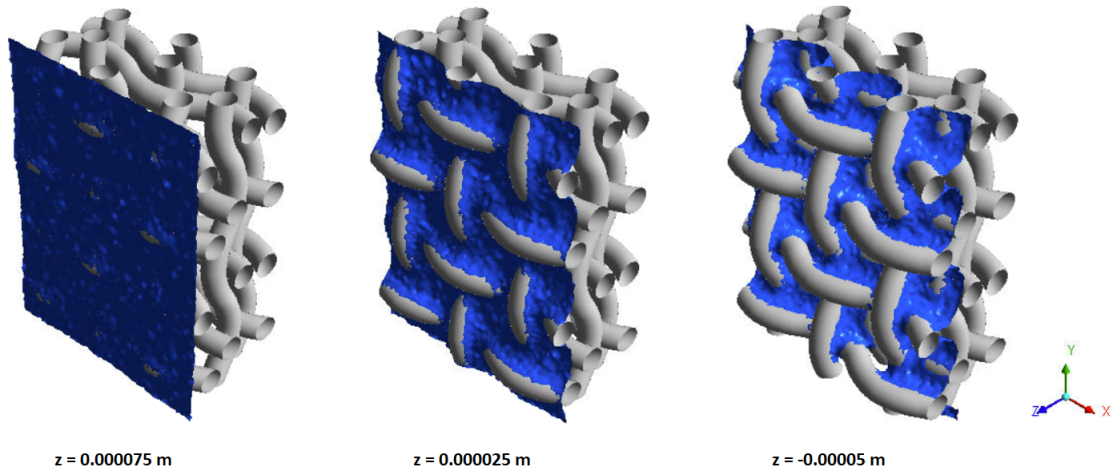

Fig. 15. Changes in the meniscus shape for a contact angle of 5^o at different saturation levels

IV. NUMERICAL SIMULATIONS: SINGLE-PHASE FLOW

Overall we seek to extract more relevant closure information, such as the friction factor and the heat transfer coefficient. The VOF simulations require an extremely small time-step of the order of 10^{-6}. Therefore, coupling them with heat transfer would be extremely computationally expensive, as diffusion is a process that requires a long time to occur. Single-phase simulations [27] with liquid in a fixed meniscus model are proposed to perform the subsequent calculations.

IV.A. Methods

IV.A.1. Model description

The highly curved meniscus shape – corresponding to the contact angle between the solid-liquid-vapor interface of 5 degrees, was chosen to develop a new model. As observed previously, this shape provides higher capillary pressure and is typical of higher temperatures within the operational range of a sodium heat pipe.

We then exported the isosurface of the liquid-vapor interface – the meniscus shape – and approximated it as a sinusoidal function using MATLAB and an optimization algorithm:

$$z(x,y) = 1e-05 \times (2.6 + 1.19sin(\pi(8000x - 0.2)) + 3.3sin(\pi(8000y - 0.125))) \tag{3}$$

In Figure 16, the two surfaces are overlapped to match the surface's minimums and maximums. The interface shape described by (IV.A.1) has an error evaluated with the least square method of less than 5%. This step made the generation of a fixed-meniscus domain feasible. Because the meniscus shape is simply a function of the capillary pressure, its curvature remains the same during simulations coupled with heat transfer [13].

The parametric surface was plotted, and the wires were removed to construct the new domain using SpaceClaim, as shown in Figure 17. A tetrahedral mesh was generated and converted later into a polyhedral mesh in ANSYS Fluent.

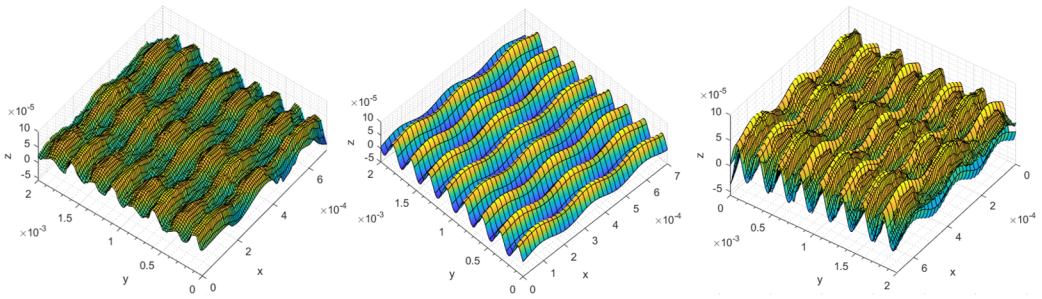

Fig. 16. Parametrization of the meniscus shape (original, parametrized and overlapped)

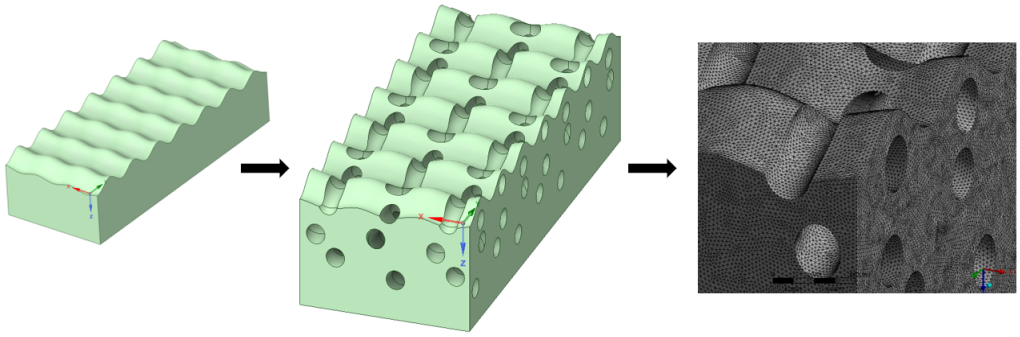

Fig. 17. Steps of the generation of the new domain and a section of its mesh

IV.A.2. Model setup

For the simulations performed in this Section, the laminar incompressible fluid flow is modeled in the domain with a fixed meniscus. We propose a simplified model consisting of a two-step simulation, in which we change the boundary condition at the interface, as described in Figure 18:

1. outflow boundary condition at the interface;
2. the velocity field is frozen, and the interface boundary condition is changed to a wall with negative heat flux.

Through this approach, we could account for the mass flowing out of the liquid domain and the heat lost due to evaporation.

For the first step, the inlet velocity is set as 0.01 m/s, and the heat flux at the wall as 112875 W/m^2, consistent with previous works with heat pipes near the outlet region of the evaporator [35]. Although it is just one choice, the work can be repeated for a broader range of parameters. We demonstrate the use of the methodology here to evaluate available correlations. A summary

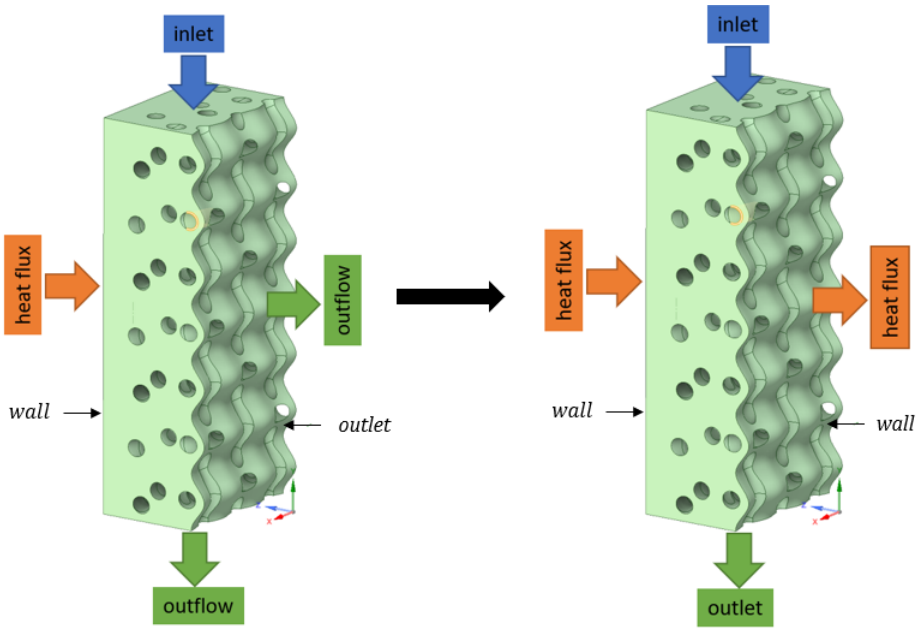

Fig. 18. Two-step simulation setup

of the parameters tested in this work is presented below.

- Inlet velocity: 0.01 m/s
- Inlet temperature: 1155, 1160, 1165, and 1170 K
- Wall heat flux: 112875 W/m^2
- Domain length: 1.41, and 2.81 mm
- Distance between wire mesh and wall: 0.1832, 0.0916, 0.0458, and 0.0229 mm

Then, the proportion of the mass flow exiting the interface in the first step was estimated as the heat transferred to the interface divided by the latent heat of vaporization:

$$\dot{m}_{interface} = \frac{q'' A_{wall}}{h_{fg}} \tag{4}$$

It resulted in an interfacial outflow of around 1-3% of the total flow rate. This estimation was in agreement with the modified Schrage Equation 5 [36] [37] for evaporation mass flow rate

through an interface, defined as:

$$\dot{m}_i^{''} = \frac{2\gamma}{2-\gamma}\sqrt{\frac{M}{2\pi R}}\frac{\rho_g h_{fg}(T_i - T_{sat})}{T_{sat}^{2/3}} \tag{5}$$

where γ is the accommodation coefficient, which in this case is 0.03, M is the molecular weight, R is the universal gas constant, T_i is the interfacial temperature, and T_{sat} is the saturation temperature, equal to 1155 K.

Then, for the second step, with the frozen velocity field, the heat flux exiting the interface was obtained by energy conservation. The results obtained after each of those steps are summarized into the Subsections IV.B.1 and IV.B.2, respectively.

IV.A.3. Mesh sensitivity study

In order to establish the mesh size, domain length, and the time step required for the simulations with the new model, a sensitivity study was performed to test the following parameters:

- Element size: $4 \times 10^{-5}m$, and $5 \times 10^{-5}m$
- Time step: 0.01 s, 0.05 s, and a steady simulation
- Domain length: $L = 1.41mm$, and $2L$

Each simulation was considered converged when the monitors of pressure, temperature, and velocity stopped changing. After this study, we decided to conduct the simulations using a mesh with the bigger element size $5 \times 10^{-5}m$ and the time step of 0.01 s. Those conditions provided a good compromise between accuracy, stability, and computational cost, with a Courant number of approximately 2. As no gravity forces are acting in this model, the domain's orientation is irrelevant, and therefore the results are presented either vertically or horizontally.

Then, we compared the case with the domain length $L = 1.41mm$ with a case twice as long. The velocity profile of those cases and the position of the planes we use to analyze the friction factor are described in Figure 19. The pressure drop is evaluated for each $0.5L$ by computing the ΔP across planes. In the graph of Figure 19, we observe that the pressure drop becomes nearly constant after a length equal to L in both simulations. This behavior shows that this domain

length is sufficient to capture the fully developed flow. Simulations are conducted at $L = 1.41mm$ for the remainder of the study.

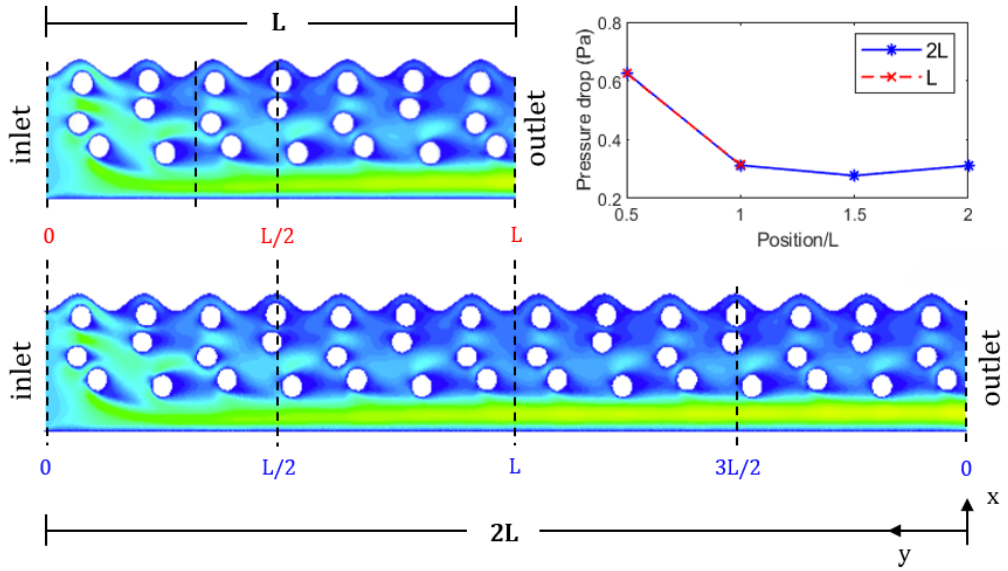

Fig. 19. Velocity field for a short (L) and a long domain (2L) with the position of some planes use in the friction factor calculation

IV.B. Results

The following two subsections present the results obtained after each of the steps of the model previously described in Subsection IV.A.2.

IV.B.1. Pressure Drop and Friction Factor

To evaluate the pressure drop, the interface is treated with outflow boundary conditions (i.e., flow split, as discussed in the previous section). Because most of the fluid flows through a liquid gap between the wire mesh and the wall, the outflow through the interface is minimal [35].

We varied the liquid gap size between the wall and the mesh wire. Even though this gap is a design parameter in annular heat pipes, it is also present in pure wick heat pipes since perfect adhesion between mesh wire and wall cannot be ensured. As the gap size changes, the porosity will also change. We then observe the liquid behavior through the domain (Figure 20) and its influence on the pressure drop (Figure 21).

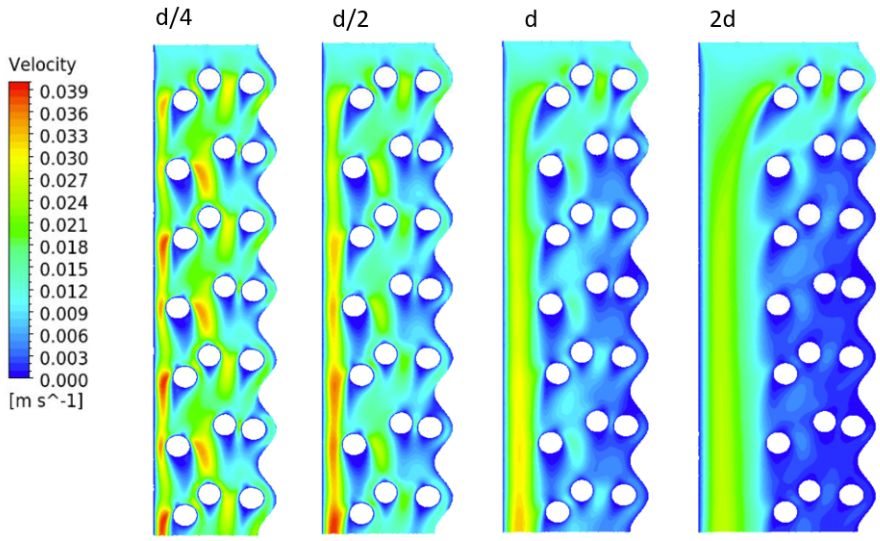

Fig. 20. Velocity field for different sizes of liquid gap

The pressure drop as a function of the liquid gap size was calculated at different domain heights to neglect the significant pressure losses at the entrance region, where the flow is not fully developed (Figure 21). In the following, the pressure drop is defined as:

$$\Delta P = P_{outlet} - P_{plane} \tag{6}$$

where the plane varies with the height in the y-direction.

As shown in Figure 21, the results are as expected: with lower pressure drop for the measurements at the smaller heights. Also, it can be observed that there is a more considerable pressure drop for the tightly packed domain and a slight pressure drop for the domain with the large liquid gap, where the flow goes mainly through this empty channel. It is also evident that the pressure drop is highly sensitive to changes in porosity.

We then compared results from the simulation and, in particular, the fully developed friction factor with available correlations. To do so, some post-processing of the simulations was needed. As previously observed, most of the flow goes through the gap between the wick and the wall. The average velocity v_l is computed in this channel between the wall and the screen mesh, marked in Figure 22 (a), to obtain a Reynolds number based on the hydraulic diameter of $2d_l$:

$$Re = \frac{\rho v_l 2 d_l}{\mu} \tag{7}$$

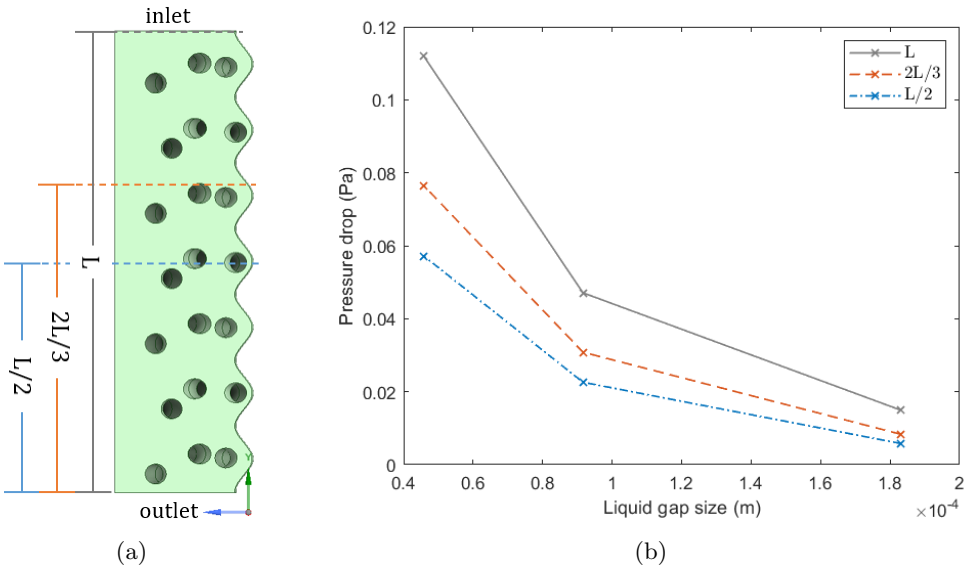

(a) (b)

Fig. 21. Pressure drop as function of the liquid gap size measured at three heights

Then, we calculated the friction factor for laminar flow in tubes:

$$f = \frac{64}{Re} \tag{8}$$

And in infinite channels (laminar channel flow):

$$f = \frac{24}{Re} \tag{9}$$

Furthermore, we calculated the friction factor using the Darcy-Weisbach correlation:

$$f = \frac{2\Delta P D_h}{L v^2} \tag{10}$$

where L was varied and consequently the ΔP. Figure 22 (a) shows the regions where the parameters were computed. This calculation did not consider the entrance region since the flow needed to be fully developed. The results are presented in Figure 22 (b), where we can observe that the laminar correlation for tubes presents a good agreement for less tightly packed channels compared to the Darcy-Weisbach correlation. However, for smaller porosities, the results are overestimated. The laminar correlation for infinite channels, however, underestimated the friction factor.

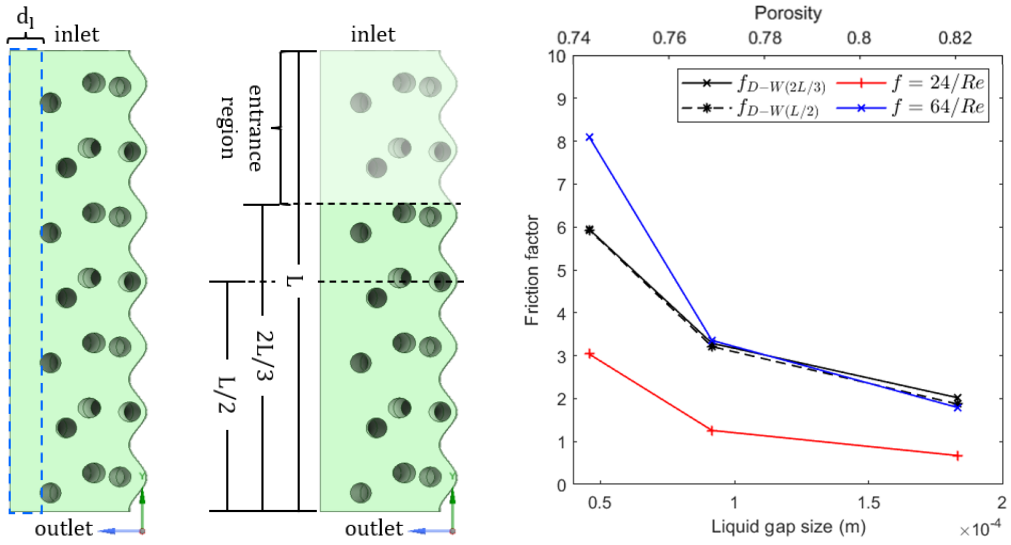

(a) (b)

Fig. 22. (a) Scheme of the regions used to compute the parameters of the friction factor, (b) Friction factor as a function of the liquid gap size

Then, we tested several well-known correlations for fluid flow through packed columns [38] [39] [40] [41]. However, most of them overestimate the friction factor for our geometry. We found a better agreement using a general correlation [42], in which we could choose coefficients better suitable for our case:

$$f = \frac{A}{Re_{dp}} \frac{(1-\epsilon)^2}{\epsilon^3} + \frac{B}{Re_{dp}^{2-n}} \frac{(1-\epsilon)^{3-n}}{\epsilon^3} \tag{11}$$

where the A and B are coefficients determined empirically. In this correlation, the coefficient A depends on the shape of the particle [41], and B depends on the ratio between the equivalent diameter of the pipe's liquid film, D, and the particle diameter, dp [43]. For this correlation, the characteristic length in the Reynolds number is dp:

$$Re_{dp} = \frac{\rho v dp}{\mu} \tag{12}$$

where dp is defined as:

$$dp = 6 \frac{\text{Volume of wire}}{\text{Area of wire}} \tag{13}$$

The term multiplying A characterizes the laminar flow, and the one multiplying B characterizes the turbulent flow. We consider the flow as laminar given that $Re_{dp} = 4.2$, and the Reynolds

coefficient is therefore set to $n = 1$. For turbulent flow ($Re_{dp} > 300$) we typically have $n = 2$. Transitional values typically follow in between [41] [40].

According to the literature [43] [42], the value of the coefficient A is 150 for spheres and 200 for cylinders. Furthermore, the coefficient B can be obtained with the following equations:

- Spheres

$$\frac{1}{\sqrt{B}} = \frac{1.5}{(D/dp)^2} + 0.88$$

- Cylinders

$$\frac{1}{\sqrt{B}} = \frac{2}{(D/dp)^2} + 0.8$$

The parameters obtained for the cases in this work are the following:

- $Re_{dp} = 4.2$
- $2.55 < D/dp < 4.2$
- $0.74 < \epsilon < 0.82$
- $A = 150 \longrightarrow 0.81 < B < 1.07$
- $A = 200 \longrightarrow 0.82 < B < 1.20$

where the porosity, ϵ is defined as:

$$\epsilon = \frac{\text{volume of the fluid}}{\text{volume of fluid without the wires}} \tag{14}$$

We also examine the sensitivity to the defined parameter n. The extreme cases for coefficients A and B were tested as bounding cases to our data. Two cases are shown in Figure 23, with n varying from 1.0 to 2.0.

Overall, a better agreement was found for the case for spheres and lower value of B, and therefore lower D/dp. The value of n for the laminar - or quasi-laminar - flow agrees with our simulation for the minor gap cases. For larger gaps, the results agree better with the correlation for laminar flows in tubes (8). Using those parameters, we can rewrite our correlation as follows:

$$f = \frac{150.81}{Re_{dp}} \frac{(1-\epsilon)^2}{\epsilon^3} \tag{15}$$

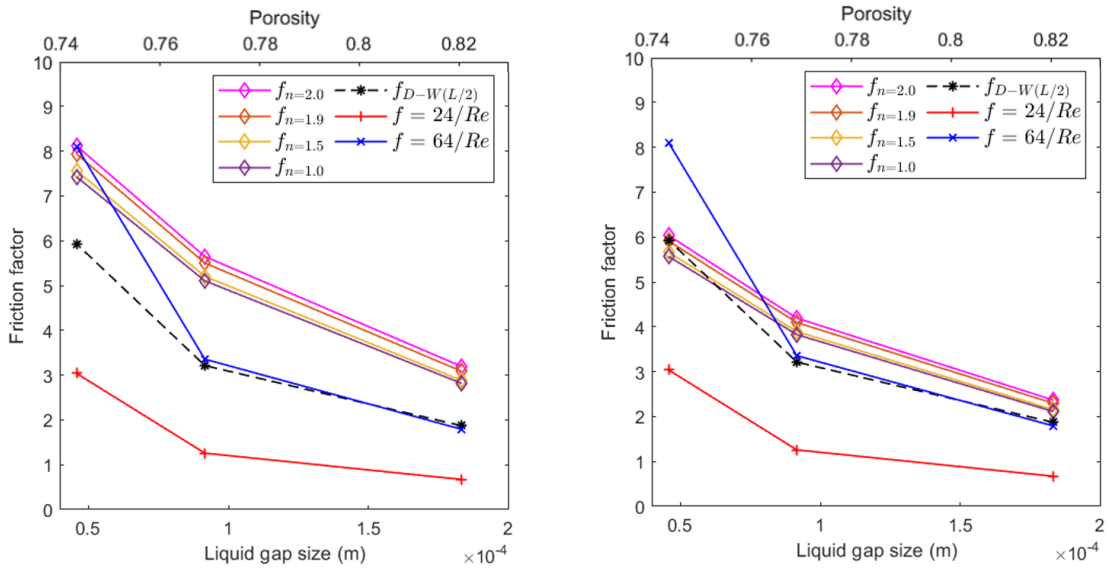

Fig. 23. Friction factor as function of the liquid gap size: (a) A = 200, and B = 1.2; and (b) A = 150, and B = 0.81

We note that this is based on a limited set of cases, but the methodology can be repeated for a larger dataset.

IV.B.2. Heat transfer coefficient

After removing the heat due to evaporation at the interface and concluding the second step of our model setup, we could perform a heat transfer analysis. *We evaluate the heat transfer coefficient at the wall and the interface.*

The evaporative heat transfer coefficient was calculated using the following correlation:

$$h_{evap} = \frac{\dot{m}_i^{''} h_{fg}}{T_i - T_{sat}} \tag{16}$$

where $\dot{m}_i^{''}$ is obtained through the Equation 5. The results are consistent with recent research [13] and yield a $h_{evap} = 6.89(W/m^2K)$.

We focus, however, on wall heat transfer. The average wall temperature T_{wall} is first computed at a given stream-wise plane to evaluate the wall heat transfer coefficient. The bulk tem-

perature T_{bulk} is also calculated at those planes:

$$T_{bulk} = \frac{\int_{\omega} T u dV}{\int_{\omega} u dV} \tag{17}$$

We then obtain the local heat transfer coefficient, given by:

$$h = \frac{q''}{T_{wall} - T_{bulk}} \tag{18}$$

And the Nusselt number is defined as:

$$Nu = \frac{h D_e}{k} \tag{19}$$

where D_e is the length of the heated wall.

The planes where the heat transfer coefficient was calculated, and the Nusselt number at those planes for one of the cases are shown in Figure 24.

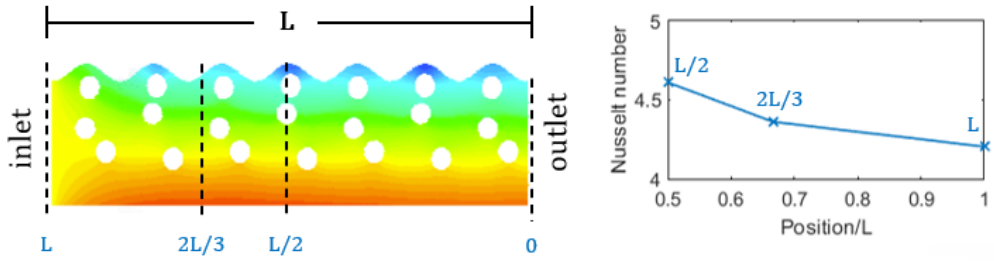

Fig. 24. Temperature field for a short domain (L) with the position of some planes used to calculate the heat transfer coefficient

The Nusselt number computed at a plane across the domain near the outlet is presented in Table VII. We observe small Nusselt numbers, varying from 2.5 to 5.2, as expected for the laminar flow of sodium. The Nusselt number is lower in the case with the smaller porosity, showing that the heat transfer occurs almost purely by conduction.

TABLE VII
Nusselt number for different liquid gap sizes

Liquid gap size	Porosity	L
2d	0.82	4.67
d	0.78	4.61
d/2	0.75	3.40
d/4	0.73	2.65

Then, the results obtained for the local wall heat transfer are compared with several correlations for liquid metals, such as Lyon [44], Aoki [45], and Skupinski et al. [46], respectively:

$$Nu = 4.0 + 0.025Pe^{0.8} \tag{20}$$

$$Nu = 5.3 + 0.019Pe^{0.8} \tag{21}$$

$$Nu = 4.82 + 0.0185Pe^{0.827} \tag{22}$$

where the Péclet number is:

$$Pe = Pr \times Re \tag{23}$$

with a Prandtl number $Pr = 0.0041$, and $Pe < 1$.

The profiles obtained for the local heat transfer coefficient and Nusselt number as a function of the position over the domain length are shown in Figure 25 (a). The dashed lines represent the heat transfer coefficient computed in the whole domain for each case. As previously observed in Table VII, the local heat transfer profiles for each case are nearly constant along its length.

Figure 25 (b) presents a comparison between the Nusselt number computed at the outlet of the smaller domain, varying the liquid gap size, and the correlations described in Equations 20, 21, and 22. Although existent heat transfer correlations are mainly derived from turbulent heat transfer data, for higher porosity, the Lyon correlation presented a good agreement with the simulation results, with a 1% difference. On the other hand, Aoki [45] and Skupinski [46] overestimated our results in 27% and 16%, respectively. Which was expected, as they are suitable for $Pe > 100$, and in our work, the Péclet number is below unity.

Comparisons with other well-known correlations for liquid metals [47] [48] [49] were also performed. However, although they presented the same trend, most of them overestimated the Nusselt number by more than 80%. We observed that heat transfer correlations dependent only on the Péclet number provided a value closer to our results.

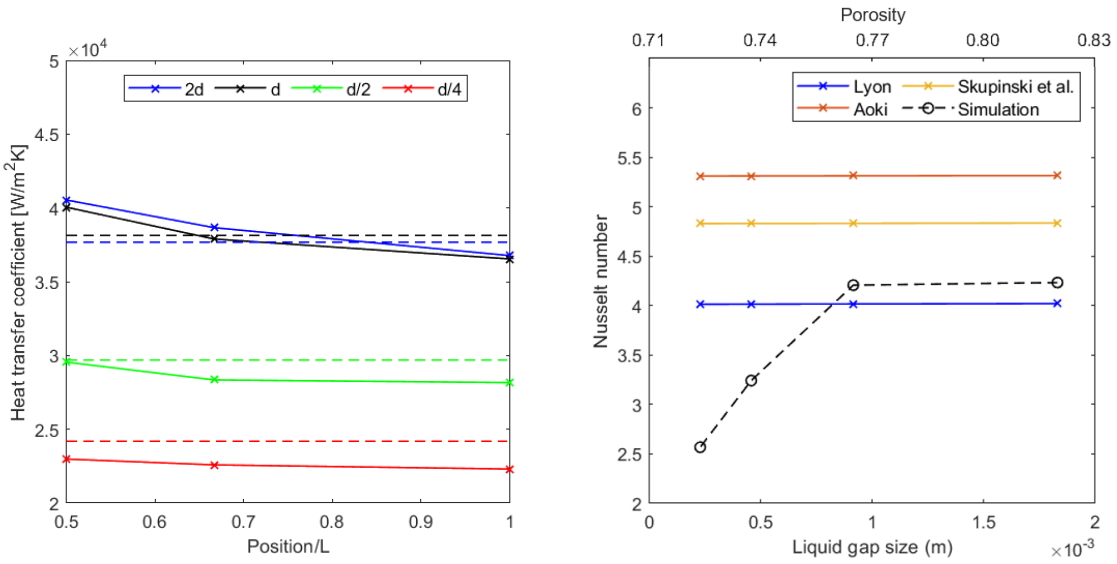

(a) (b)

Fig. 25. (a) Heat transfer coefficient and (b) Nusselt number as function of the Position over the total length

Finally, three values of inlet superheat $\Delta T = 5, 10$, and $15K$ were investigated in Table VIII. The change in the Nusselt number is expected to be minimal, as the local heat transfer coefficient value is practically independent of the heat flux imposed on the wall. This trend was in agreement with the literature [13] [15].

TABLE VIII
Nusselt number for different super heats and positions along the domain

ΔT	L/2	2L/3	L
0 K	4.21	4.36	4.61
5 K	4.15	4.32	4.58
10 K	4.15	4.31	4.57
15 K	4.15	4.29	4.58

V. NUMERICAL SIMULATIONS: SOCKEYE

The operational range of the heat pipe is determined by its limitations to heat transport, such as capillary and sonic limits. The capillary limit depends on the design of the wick, which affects the heat pipe capability of pumping liquid from the condenser to the evaporator. To maintain the

appropriate operation of the heat pipe, the capillary pressure must be greater or equal to the sum of pressure losses for liquid, vapor, phase changes, and gravity. Among those, the pressure drop of the liquid due to the frictional drag can be more significant depending on the operating conditions [50].

In order to increase the maximum heat transfer at which a heat pipe can operate, the design of the wick must be considered. For example, porosity, permeability, and liquid gap size changes can affect the maximum attainable capillary pressure [51]. This part of the work aims to validate Sockeye simulations of a heat pipe model against the experiments discussed in Section II. We also compare numerically evaluated capillary limit curves for the same model against available capillary limit curves provided in the literature.

V.A. Methods

The experimental setup and the numerical study data are utilized to model the heat pipe. Here, the 2-D model is built using the MOOSE framework application Sockeye [9], which accounts for the liquid and vapor flow inside the heat pipe and the heat conduction through its stainless steel envelope. The external dimensions of the heat pipe, with the evaporator, adiabatic, and condenser sections, as well as the heat input and removal, are obtained from the experiments in Section II. The wall heat transfer coefficient and design information on the wick, derived from Sections III, and IV, is used to calculate the pore radius, given by [51]:

$$r_{eff} = \frac{1}{2N} \tag{24}$$

Where N is the number of holes in the screen mesh per meter and the permeability:

$$K = \frac{d^2\epsilon^3}{122(1-\epsilon)^2} \tag{25}$$

where d is the wire diameter.

V.B. Results

The wall temperature across the axial position was computed using a pore radius of 1.25 $\times 10^{-4} m$, permeability of 3.04 $\times 10^{-10} m^2$, and a fixed porosity of 0.76. The placement of the

thermocouples in the experiment caused temperature differences due to their thermal resistance to the heat pipe wall. Those differences were simulated with ANSYS Fluent by modeling the setup of the heater and the heat exchanger around the heat pipe. The results were incorporated into the temperature distribution obtained with Sockeye. Once compared to the experiments, as shown in Figure 26, the simulations yielded a remarkable degree of agreement.

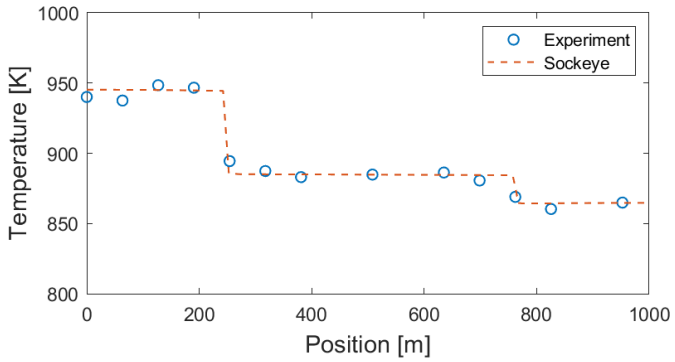

Fig. 26. Validation of the wall temperature for Test-018

After validating the Sockeye model, the power input was increased until the void fraction in the evaporator was larger than in the interface, characterizing a dry-out of the wick. The cases tested are presented in Table IX, using initial temperatures ranging from 900 to 1600K.

The first three cases, depicted in Figure 27 (a), were performed by changing the liquid gap size until obtaining a limit curve close to the one provided by the heat pipe vendor, Advanced Cooling Technologies [18]. In those cases, the liquid friction factor correlation utilized by Sockeye is for annular flows, given by:

$$\frac{24}{Re}\left(\frac{D_{wick,o}}{D_{hp,i}}\right)^{0.035} \tag{26}$$

where $D_{wick,o}$ is the outer diameter of the wick and $D_{hp,i}$ is the inner diameter of the heat pipe. However, as the fraction of these two parameters is nearly 1, this correlation can be approximated by the friction factor for laminar flow, presented in the previous section, in Equation 9.

In the other cases, shown in Figure 27 (b), the liquid friction factor was changed, and the liquid gap size was fixed. The correlation presented in Section IV, in Equation 15, was compared to the default correlation of Sockeye and the friction factor for laminar flows in tubes 8.

The results presented in Figure 27 (a) show that the capillary limit increases with the liquid gap size. Figure 27 (b) shows the influence of the choice of liquid friction factor correlation in the

TABLE IX
Cases tested in the calculation of the capillary limit

Test	Liquid gap size [mm]	Friction factor correlation
01	0.0918	$\frac{24}{Re}\left(\frac{D_{wick,o}}{D_{hp,i}}\right)^{0.035}$
02	0.1836	$\frac{24}{Re}\left(\frac{D_{wick,o}}{D_{hp,i}}\right)^{0.035}$
03	0.1262	$\frac{24}{Re}\left(\frac{D_{wick,o}}{D_{hp,i}}\right)^{0.035}$
04	0.2525	$\frac{24}{Re}\left(\frac{D_{wick,o}}{D_{hp,i}}\right)^{0.035}$
05	0.2525	$\frac{150.81}{Re_{dp}}\frac{(1-\epsilon)^2}{\epsilon^3}$
06	0.2525	$\frac{64}{Re}$

capillary limit. The correlation presented in this paper, in Test 05, presented a lower capillary limit even with a relatively large liquid gap.

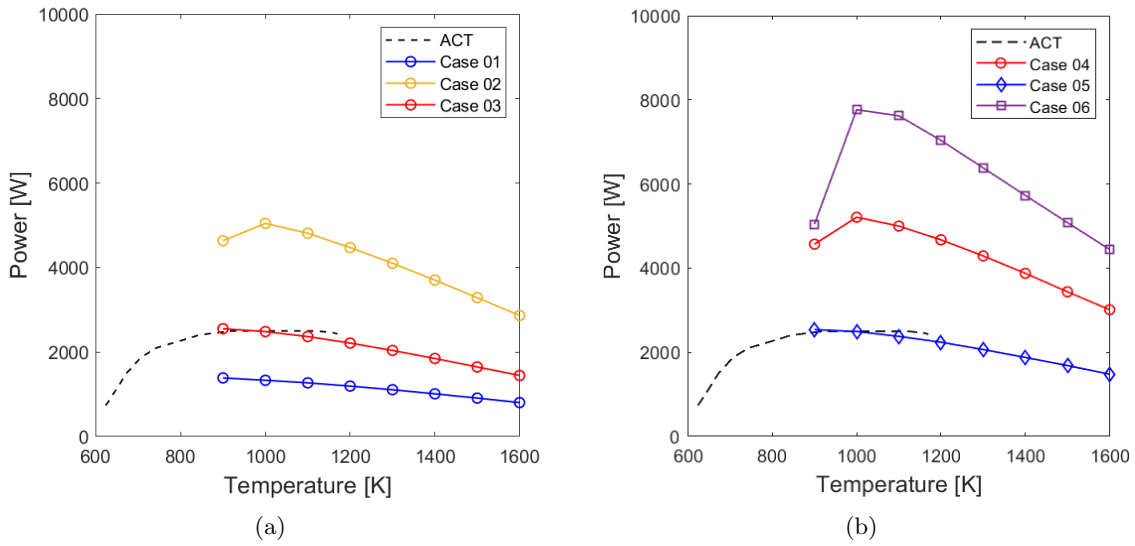

(a) (b)

Fig. 27. Capillary limit for: (a) Tests 01 - 03, with different liquid gap sizes, and (b) Tests 04 - 06, with different liquid friction factor correlations

VI. CONCLUSION

This manuscript discussed a fundamental study of the physics of liquid metal heat pipes. We presented unique experimental and numerical data for model validation, supporting the advancement of best-estimate analysis codes needed to perform safety analyses of Heat Pipe Microreactors.

In the initial modeling work, results obtained with VOF have been leveraged to evaluate the capillary pressure as a function of saturation level in the wick and contact angle. The simulations performed with water yielded numerical results in agreement with the literature. Novel results with sodium allow us to establish a basis for evaluating closure relationships in liquid metal heat pipes.

In the second step of the numerical campaign, single-phase simulations were performed in a new domain with a fixed interface. The focus is on the liquid flow within the wick and the associated friction and heat transfer. Friction factor correlations were tested for several cases varying the wick-to-wall gap of the domain. We note that the pressure drop is very sensitive to the wall-wick gap size overall. Although there is a lack of correlations for this particular geometry, we observed some agreement when comparing friction factor correlations for packed spheres in a liquid column. Darcy channel flow correlations, often used for liquid metal heat pipes with annular gaps, are a good approximation only for relatively large gaps. We also evaluated heat transfer correlations for wall heat transfer.

In the final part of the numerical study, results obtained in Sockeye are briefly presented. The calculations with Sockeye are performed using the experimental setup parameters and information from the previous numerical simulations, such as the wick characteristics and the wall heat transfer coefficient. The experiments validate the results, and the capillary limits are obtained for several cases. These results build confidence in the capability of Sockeye to compute the temperature distribution in heat pipes and predict the capillary limit. They also highlight the importance of the liquid friction factor correlation.

For future work, the parameters tested here will be expanded to cover a broader range of non-dimensional numbers. We are also currently exploring the other regions of the heat pipe, numerically, such as the vapor core, the condenser, and the liquid-vapor coupling through the fixed meniscus interface, with more accuracy. The correlations obtained from these multiple approaches will be implemented within Sockeye [9]. The proposed next steps for the experimental work will

focus on X-ray radiography of the heat pipe and detailed high-resolution temperature experiments.

Ultimately, one of the project's goals is to augment Sockeye with the newly developed correlations and further improve the existing Sockeye models of the University of Michigan experiments. Results will be compared against additional experimental data and used to help validate the overall modeling approach for normal operation and close to the operational limits.

ACKNOWLEDGMENTS

This project was supported in part by the U.S. Nuclear Regulatory Commission.

We would like to thank Dr. Joshua Hansel from Idaho National Laboratory for the support in setting up the numerical models in Sockeye.

REFERENCES

[1] J. Kennedy, "Special Purpose Application Reactors: Systems Integration Decision Support," *INL/EXT-18-51369* (2018).

[2] R. Testoni, A. Bersano, and S. Segantin, "Review of nuclear microreactors: Status, potentialities and challenges," *Progress in Nuclear Energy*, **138**, 103822 (2021).

[3] C. Matthews, V. Laboure, M. DeHart, J. Hansel, D. Andrs, Y. Wang, J. Ortensi, and R. C. Martineau, "Coupled Multiphysics Simulations of Heat Pipe Microreactors Using DireWolf," *Nuclear Technology*, **207**, *7*, 1142 (2021).

[4] H. Jouhara, A. Chauhan, T. Nannou, S. Almahmoud, B. Delpech, and L. Wrobel, "Heat pipe based systems - Advances and applications," *Energy*, **128**, 729 (2017).

[5] A. Faghri, "Heat pipes: Review, opportunities and challenges," *Frontiers in Heat Pipes*, **5** (2014).

[6] D. Shaver and A. Tentner, "Initial Evaluation of Nek-2P for Modeling of Liquid Metal Heat Pipes," , ANL/NSE-19/42 (2019).

[7] A. B. Solomon, K. Ramachandran, L. G. Asirvatham, and B. C. Pillai, "Numerical analysis of a screen mesh wick heat pipe with Cu/water nanofluid," *International Journal of Heat and Mass Transfer*, **75**, 523 (2014).

[8] R. Ranjan, J. Y. Murthy, S. V. Garimella, and U. Vadakkan, "A numerical model for transport in flat heat pipes considering wick microstructure effects," *International Journal of Heat and Mass Transfer*, **54**, *1-3*, 153 (2011).

[9] J. E. Hansel, R. A. Berry, D. Andrs, M. S. Kunick, and R. C. Martineau, "Sockeye: A One-Dimensional, Two-Phase, Compressible Flow Heat Pipe Application," *Nuclear Technology*, 1–22 (2021).

[10] K. K. Bodla, J. Y. Murthy, and S. V. Garimella, "Direct simulation of thermal transport through sintered wick microstructures," *Journal of Heat Transfer*, **134**, *1* (2012).

[11] K. K. Bodla, J. Y. Murthy, and S. V. Garimella, "Evaporation analysis in sintered wick microstructures," *International Journal of Heat and Mass Transfer*, **61**, *1*, 729 (2013).

[12] R. Kempers, D. Ewing, and C. Y. Ching, "Effect of number of mesh layers and fluid loading on the performance of screen mesh wicked heat pipes," *Applied Thermal Engineering*, **26**, 589 (2006).

[13] X. Chen, C. Qi, W. Wang, J. Miao, and H. Zhang, "Investigation of interface profiles in meshed wicks and related evaporation characteristics," *International Journal of Thermal Sciences*, **177**, *July 2021*, 107522 (2022).

[14] R. Kempers, A. Robinson, D. Ewing, and C. Ching, "Characterization of evaporator and condenser thermal resistances of a screen mesh wicked heat pipe," *International Journal of Heat and Mass Transfer*, **51**, *25-26*, 6039 (2008).

[15] D. Khrustalev and A. Faghri, "Heat transfer during evaporation on capillary-grooved structures of heat pipes," *Journal of Heat Transfer*, **117**, *3*, 740 (1995).

[16] C. W. Hirt and B. Nichols, "Journal of computational physics," *Journal of Heat Transfer*, **39**, *1*, 201 (1981).

[17] P.-H. Huang, T. Ahn, A. Manera, and V. Petrov, "Design of a sodium heat pipe experimental setup for the special purpose nuclear reactor," *Proceeding of ANS online meeting* (2021).

[18] T. Ahn, P.-H. Huang, A. Manera, and V. Petrov, "Experimental study on startup characteristics of a sodium-filled heat pipe, using in-house high-resolution and high-speed radiation-based imaging system," *Proceeding of NURETH-19*, Brussels, Belgium (2022).

[19] P. Sabharwall, C.-S. Lin, J. E. Hansel, V. Laboure, D. Andrs, W. M. Hoffman, S. R. Novascone, A. E. Slaughter, and R. C. Martineau, "Integrated Modeling and Simulation Capability for Full Scale Multi-Physics Simulation and Visualization of MicroReactor Concept," (INL/EXT-19-55159), Idaho National Laboratory (INL), United States (2019).

[20] Z. Tian, C. Wang, D. Zhang, L. Xiao, W. Tian, S. Qiu, and G. H. Su, "Experimental investigation on the heat transfer performance of high-temperature potassium heat pipe for nuclear reactor," *Nuclear Engineering and Design*, **378**, 111182 (2021).

[21] C. Wang, L. Zhang, L. Xiao, S. Tang, S. Qiu, and G. H. Su, "Experimental study on startup performance of high temperature potassium heat pipe at different inclination angles and input powers for nuclear reactor application," *Annals of Nuclear Energy*, **136**, 107051 (2020).

[22] L. H. R. Cisterna, F. H. Milanez, and M. B. H. Mantelli, "Prediction of geyser boiling limit for high temperature two-phase thermosyphons," *International Journal of Heat and Mass Transfer*, **165**, 120656 (2021).

[23] Dassault Systemes SolidWorks Corp., "Solidworks," URL https://www.solidworks.com.

[24] B. Ch Nookaraju, P. Keziya Rani, P. Kurmarao, S. Naga Sarada, N. Sateesh, A. Anitha Lakshmi, and R. Subbiah, "Experimental and transient thermal analysis of screen mesh wick heat pipe," *Materials Today: Proceedings* (2021).

[25] W. S. Chang, "Porosity and Effective Thermal Conductivity of Wire Screens," *Journal of Heat Transfer*, **112**, *1*, 5 (1990).

[26] J. VanSant and J. Malet, "Thermal conductivity of some heat pipe wicks," *Letters Heat Mass Transfer*, **2**, 199 (1975).

[27] ANSYS, Inc., "Ansys Fluent," URL https://www.ansys.com.

[28] J. U. Brackbill, D. B. Kothe, and C. Zemach, "A continuum method for modeling surface tension," *Journal of Computational Physics*, **100**, *2*, 335 (1992).

[29] E. Merzari, H. Ninokata, S. Wang, and E. Baglietto, "Numerical simulation of free-surface vortices." *Nuclear technology*, **165**, *3*, 313 (2009).

[30] J. W. Taylor and S. D. Ford, "Solid Metal-Liquid Metal Interaction Studies. Part II. Contact Angle Relationships for Sodium on Solids," , Atomic Energy Research Establishment, AERE, Harwell (1955).

[31] M. Bader and C. A. Busse, "Wetting by sodium at high temperatures in pure vapour atmosphere," *Journal of Nuclear Materials*, **67**, 295 (1977).

[32] E. Hodkin, D. Mortimer, and M. Nicholas, "The wetting of some ferrous materials by sodium," *Liquid Alkali Metals*, 167–170, Thomas Telford Publishing.

[33] B. Longson and J. Prescott, "Some experiment on the wetting of stainless steel, nickel and iron in liquid sodium." , UKAEA, Risley Engineering and Materials Laboratory (1973).

[34] J. K. Fink and L. Leibowitz, "Thermodynamic and transport properties of sodium liquid and vapor," ANL/RE-95/2-94649, Argonne National Laboratory (ANL), United States.

[35] J. E. Hansel, R. A. Berry, D. Andrs, and R. C. Martineau, "Sockeye: A 1-D heat pipe modeling tool," INL/EXT-19-55742, Idaho National Laboratory (INL), United States (2019).

[36] R. W. Schrage, *A Theoretical Study of Interphase Mass Transfer*, Columbia University Press, New York Chichester, West Sussex (1953).

[37] T. Wen, L. Lu, W. He, and Y. Min, "Fundamentals and applications of CFD technology on analyzing falling film heat and mass exchangers: a comprehensive review," *Applied Energy*, **261**, 114473 (2020).

[38] E. Ozahi, M. Y. Gundogdu, and M. Ö. Carpinlioglu, "A modification on Ergun's correlation for use in cylindrical packed beds with non-spherical particles," *Advanced Powder Technology*, **19**, *4*, 369 (2008).

[39] C. G. Toit, P. J. V. Loggerenberg, and H. J. Vermaak, "An evaluation of selected friction factor correlations and results for the pressure drop through random and structured packed beds of uniform spheres," *Nuclear Engineering and Design*, **379**, *February*, 111213 (2021).

[40] P. C. Carman, "Permeability of saturated sands, soils and clays," *The Journal of Agricultural Science*, **29**, *2*, 262 (1939).

[41] S. Ergun, "Fluid flow through packed columns," *Chem. Eng. Prog.*, **48**, 89 (1952).

[42] B. Eisfeld and K. Schnitzlein, "The influence of confining walls on the pressure drop in packed beds," *Chemical Engineering Science*, **56**, *14*, 4321 (2001).

[43] W. Reichelt, "Zur Berechnung des Druckverlustes einphasig durchströmter Kugel-und Zylinderschüttungen," *Chemie Ingenieur Technik*, **44**, *18*, 1068 (1972).

[44] R. N. Lyon, "Liquid-metals handbook," , Committee on the Basic Properties of Liquid Metals, Office of Naval Research (1952).

[45] S. Aoki, "A consideration on the heat transfer in liquid metal." *Bulletin of the Tokyo Institute of Technology*, **54** (1963).

[46] E. Skupinski, J. Tortel, and L. Vautrey, "Determination des coefficients de convection d'un alliage sodium-potassium dans un tube circulaire," *International Journal of Heat and Mass Transfer*, **8**, *6*, 937 (1965).

[47] W. Pfrang and D. Struwe, *Assessment of correlations for heat transfer to the coolant for heavy liquid metal cooled core designs*, vol. 7352, Citeseer (2007).

[48] J. P. Hartnett and T. F. Irvine Jr, "Nusselt values for estimating turbulent liquid metal heat transfer in noncircular ducts," *AIChE Journal*, **3**, *3*, 313 (1957).

[49] K. Mikityuk, "Heat transfer to liquid metal: review of data and correlations for tube bundles," *Nuclear Engineering and Design*, **239**, *4*, 680 (2009).

[50] A. Faghri, *Heat pipe science and technology*, Global Digital Press (1995).

[51] B. Zohuri, *Heat pipe design and technology*, Springer (2011).